A Cantaloupe-Rind-Inspired Nanostructured Textile Catalyst for Enhanced and Recoverable Performance in High-Temperature Electrochemical Cells [*]

Shigekazu HIDAKA Yoshifumi MAEGAWA Yasutomo GOTO
Takumi OKAMOTO Shougo HIGASHI Yasuyuki HIKITA

Electrodes with a maximal active site density are critical for high-performance high-temperature electrochemical cells (HTECs). One widely employed approach involves the use of porous nanostructures with a high surface-to-volume ratio. However, their active site densities inevitably decrease owing to particle aggregation induced at high temperatures, necessitating further development of electrode processing techniques. Taking Pt/yttria-stabilized zirconia (YSZ) interface as a model system, a Pt nanostructured textile akin to the cantaloupe-rind pattern with high mechanical integrity is fabricated. Application of an AC voltage to this textile electrode at an elevated temperature reduces the Pt particle size from submicron to 10–80 nm forming a nanocomposite with YSZ, accompanied by a 40-fold increase in current density under high-temperature water electrolysis conditions. Furthermore, the AC voltage application to a partially aggregated electrode restores its nano-blended structure associated with the recovery of its activity. This technique is effective in counteracting particle aggregation on demand, providing an alternative approach to achieve high performance and extended lifetimes in HTECs.

Key words :
electrical treatments, in situ synthesis, nanocomposite electrodes, nanostructured textiles, particle aggregation, solid oxide electrolysis cells, triple phase boundaries

1. Introduction

Metal catalyst/oxide electrolyte interfaces are critical structures in high-temperature electrochemical cells (HTEC) such as automotive gas sensors and solid-oxide cells for energy conversions 1)–5).

Typically, such cells consist of an ion-conducting electrolyte sheet inserted between two electrodes, each coated with a catalyst that promotes the oxidation and reduction of chemicals, respectively. The impinging gas species react at the triple phase boundary (TPB), defined as the region of the catalyst interfacing the electrolyte and the reactant, and the generated ions are transported across the electrolyte to complete the reaction on the opposite electrode. In contrast to electrodes in liquid cells, the low supply of reactants and the limited surface diffusion length of the ions call for high-performance HTEC electrodes to host porous composites consisting of interconnected nanometer-sized catalysts penetrated with electrolyte ceramic grains 6).

A common outstanding challenge in such nanocomposite electrodes is the aggregation of particles due to prolonged heating cycles during fabrication and long-term operation. Exposure to high temperatures inevitably reduces the active catalyst/electrolyte interface density and accumulates stress in the structure leading to crack formation, thus limiting the performance of the cells and shortening their lifetimes 7)–10). Previous approaches to minimize particle aggregation have focused on controlling the catalyst particle size during electrode fabrication, such as the use of ultrafine particles in the initial fabrication step 11)12), or additives to limit grain-growth of the catalyst through preferential segregation at the catalyst/electrolyte boundaries 13)–15). However, considering that particle aggregation is a thermally driven process that is more pronounced for smaller particles, as demonstrated by Ryll *et al.* in the Pt/yttria-stabilized zirconia (YSZ) interface16), alternative approaches beyond the fabrication of fine particles need to be developed. In this context, the application of electrical voltage as an independent means to counteract particle aggregation is instructive17)18). For example, Zhang *et al.* applied an alternating current (AC) voltage at high temperatures to a sputtered gold (Au) electrode on YSZ to actively disassemble and mix Au and YSZ at their interface on the nanometer scale, thus significantly increasing its interface density17). Given that AC voltage is a readily accessible and controllable parameter in HTECs, it offers a promising approach not only for achieving high TPB densities but also for potentially reactivating particle-aggregated composites after high-temperature operation.

To fully exploit the benefit of AC voltage application, the entire catalyst layer must exhibit structural continuity to ensure efficient electrical conduction for effective catalyst/electrolyte blending. A uniform thick stack of nanoparticles provides structural continuity, but the surface layers far from the oxide electrolyte do not experience structural changes by AC voltage. Conversely, small catalyst loading leads to discontinuity in the catalyst particles and hence to loss of conductivity. Therefore, a new sub microstructural platform is strongly required.

In this study, inspired by the ideal 2D continuous network observed in the cantaloupe rind, we have artificially reproduced such a nanostructure. Specifically, we employed a fibrous nanostructured textile composed of continuous arrays of aggregated Pt nanoclusters and annealed it to achieve the cantaloupe rind feature. This structure allowed us to propagate the AC voltage throughout the textile structure19)–21). This textile electrode was attached to the YSZ and

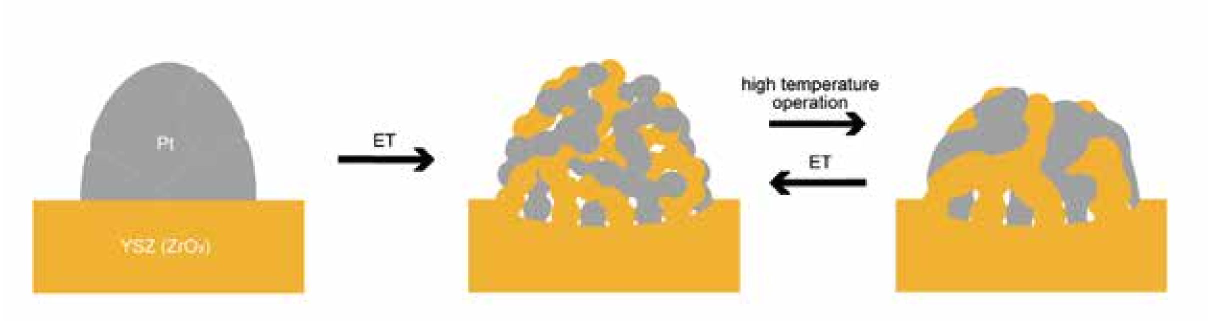

Fig. 1 Transformation of the 2D network Pt catalyst into nanocomposite active electrode via electrical treatment (ET) at high temperature. ET involved a sequential application of positive and negative voltage for 1 min repeated 20 times. The inter-diffused Pt, Zr, and O structure creates a high density of TPBs. In situ application of ET transforms an aggregated structure after high-temperature operation back to the nanocomposite structure

---

[*] Advanced Materials Interfaces 2024, 2400345 より転載 , Supporting Information はリンク先参照；https://onlinelibrary.wiley.com/action/downloadSupplement?doi=10.1002%2Fadmi.202400345&file=admi1268-sup-0001-SuppMat.pdf

subsequently subjected to an AC voltage, referred to as electrical treatment (ET), and its structural evolution was systematically investigated. We chose Pt/YSZ as a model system, as it is the most well-studied and widely utilized catalyst/electrolyte system in HTECs[22)–26)]. We examined the effect of ET on the cell performance by executing a high temperature steam electrolysis reaction, taking advantage of the high catalytic activity of Pt and the high ionic conductivity of YSZ. The Pt nanostructured textile enabled the effective application of ET to produce a porous 3D nanocomposite consisting of a uniform blend of Pt, Zr, and O. This structure resulted in a 40-fold increase in the cell output, approaching the highest among the Pt/YSZ system. Moreover, the application of ET on a partially degraded electrode led to the successful recovery of its activity, providing a readily accessible method to overcome particle aggregation on demand (Fig. 1). These results were described by using a simple model that connects the electrode microstructures with the macroscopic output of the cell, presenting a guideline for designing high-performing HTEC electrodes[11)–14)].

2. Results and Discussion

As shown in Fig.2a, the nanostructured textile electrode was fabricated by electrospinning polyvinylpyrrolidone (PVP) to form a nanostructured layer on a metal plate, followed by sputtering with Pt metal. The Pt-sputtered PVP nanostructured layer was peeled off from the metal plate and immersed in water to release the Pt nanostructured textile by selective dissolution of the underlying PVP, and subsequently attached to the YSZ substrate for further characterization (see Experimental Section for details). The deposited Pt mass of 0.6 mg cm^{-2} was much lower than that of typical electrodes (≈10 mg cm^{-2}) used in screen printing to ensure the effective application of the electric field to the Pt/YSZ interface [27)28)]. As shown in the scanning electron microscopy (SEM) image in Fig. 2b, the as-grown Pt nanostructured textile electrode consists of fibrous aggregates of 5–25 nm-sized Pt nanoclusters, similar to the metal nanoclusters reported by Higashi *et al* [19)–21)]. By heating the as-attached electrode on the YSZ substrate at 500 °C for 1 h, slight fusion in the Pt nanoclusters of the fibrous structure was observed (Figure S1, Supporting Information). Further annealing at 950 °C for 1 h drastically changed the fibrous structure to a 2D network structure akin to the pattern of a cantaloupe rind (Fig. 2c). Given that the melting point of Pt is 1775 °C, the observed textural transitions at 500 and 950 °C are consistent with the onset of surface diffusion at temperatures one-third to one-half of the melting point and diffusion-driven grain growth in proximity to the melting point, respectively [29)30)]. Despite its markedly fine and porous 2D network, the coarsening of the fibrous structure upon heating led to a >15-fold reduction in its in-plane electrical resistivity from the as-attached value of 340 to 22 Ω cm. The obtained low resistivity, comparable to that of the bulk (10 Ω cm, Ref [31)].), combined with its uniform continuous structure established a solid foundation for the subsequent application of ET.

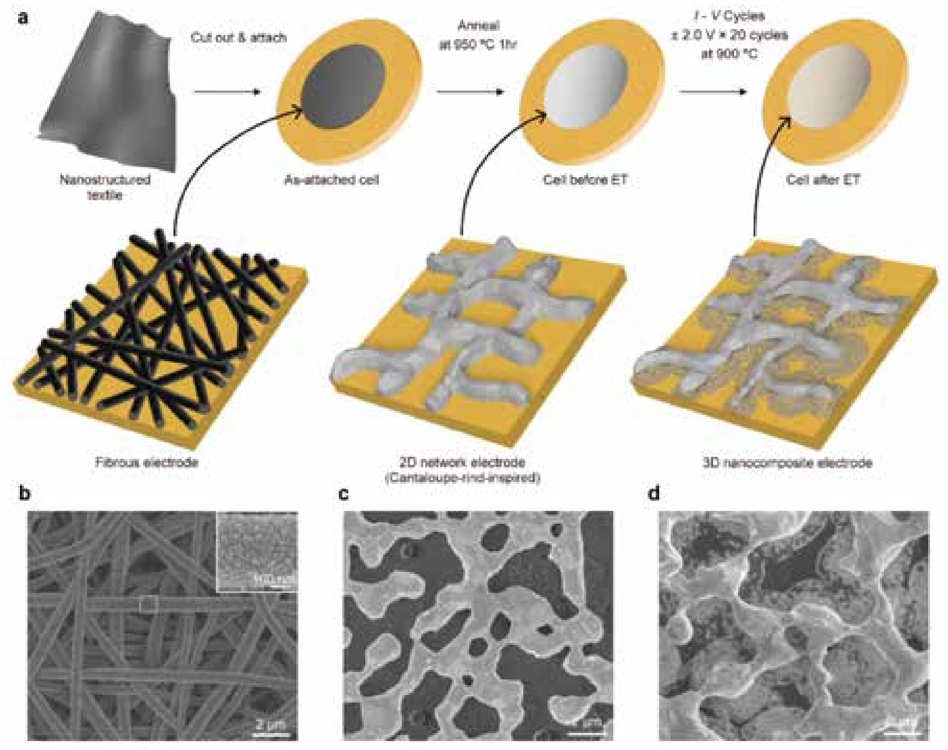

Fig. 2 Schematics of the nanostructured textile electrode fabrication process and the fabricated electrodes observed using SEM. a) Nanostructured textile electrode fabrication process. Schematics of the electrode microstructures at each step are shown. b–d) SEM observation of the electrode as attached (b), after annealing at 950℃ for 1 h producing the cantaloupe-rind pattern (c), and after subsequent electrical treatment (ET) at 900 ℃ under an applied voltage V_{ET} of 2.0 V (d). The inset in (b) is a magnified view of the fibrous structure. The bright and dark region in (c) and (d) corresponds to the Pt and the YSZ region, respectively

A single ET process involved the application of ± 2.0 V every 1 min repeated 20 times, with Pt as the positive terminal (see Experimental procedures for details). By conducting ET to the 2D network Pt electrode at 900 °C, dispersive microparticles were uniformly generated along the Pt/YSZ interface as can be observed from the plan-view SEM in Fig. 2d. In order to gain elemental insights on the atomic scale, a cross-sectional scanning transmission electron microscopy-energy dispersive X-ray spectroscopy (STEM-EDS) was measured. The Pt/YSZ interface of the 2D network reveals a sharp interface with minimal interdiffusion of elements at the interface (Fig. 3a). In contrast, this interface transforms into a 3D nanocomposite structure with the nanoparticles consisting of Zr and O, diffused through the Pt particle cracks after the ET process (Fig. 3b). Compared to similar electric-field-induced nanoparticles in other systems [32)–35)], the 3D nanocomposite generated in this study was significantly finer and more dispersed over a wide area. This owes to the continuous nature of the Pt 2D network textile, maximizing the Pt/YSZ interface density over which the voltage was applied.

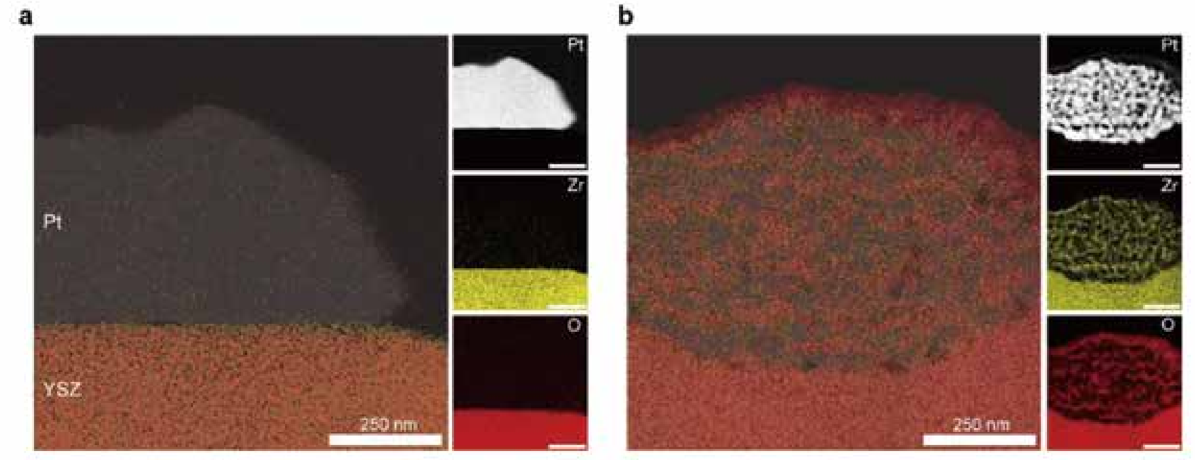

Fig. 3 STEM-EDS results of the Pt/YSZ cross-sectional interface before and after ET. a) An overlaid elemental map of the Pt/YSZ interface before ET with Pt in white, Zr in yellow, and O in red. b) An overlaid elemental map of the Pt/YSZ interface after ET with Pt in white, Zr in yellow, and O in red. The scale bars in elemental maps are 250 nm

To evaluate the effect of micro-structuring on the cell performance, the current–voltage (*I-V*) characteristics were measured under steam electrolysis conditions (Fig. 4a). A substantial increase in current density was observed for the cells after ET at all temperatures. Such enhancement is a consequence of increased TPB density, as schematically illustrated in Fig. 4a (inset), as confirmed by the electrochemical impedance spectroscopy results (Fig. 4b; Figure S2, Supporting Information), revealing reduced polarization resistance (*R*p) by approximately a factor of four while maintaining a low series resistance of 9.5 Ω even after ET. Subjecting this ET-processed cell for 10 h under a constant current density of 100 mA cm^{-2} at 800 °C, the cell voltage increased by 7.7% from 1.23 to 1.33 V (Fig. 4c), which was accompanied by the disappearance of dispersed microparticles, and the emergence of aggregated micrometer-sized domains as directly observed from the SEM image (Fig. 4d). The execution of ET to this degraded cell successfully led to the recovery of the Rp to its initial value through the re-transformation of the aggregated electrode back into a 3D nanocomposite with dispersed microparticles as shown in Fig. 4e, resembling the initial structure after ET in Fig. 2d. This series of experiments clearly demonstrates the unique capability of ET to reactivate the cell performance on demand under operating conditions without disassembly and replacement of the electrode.

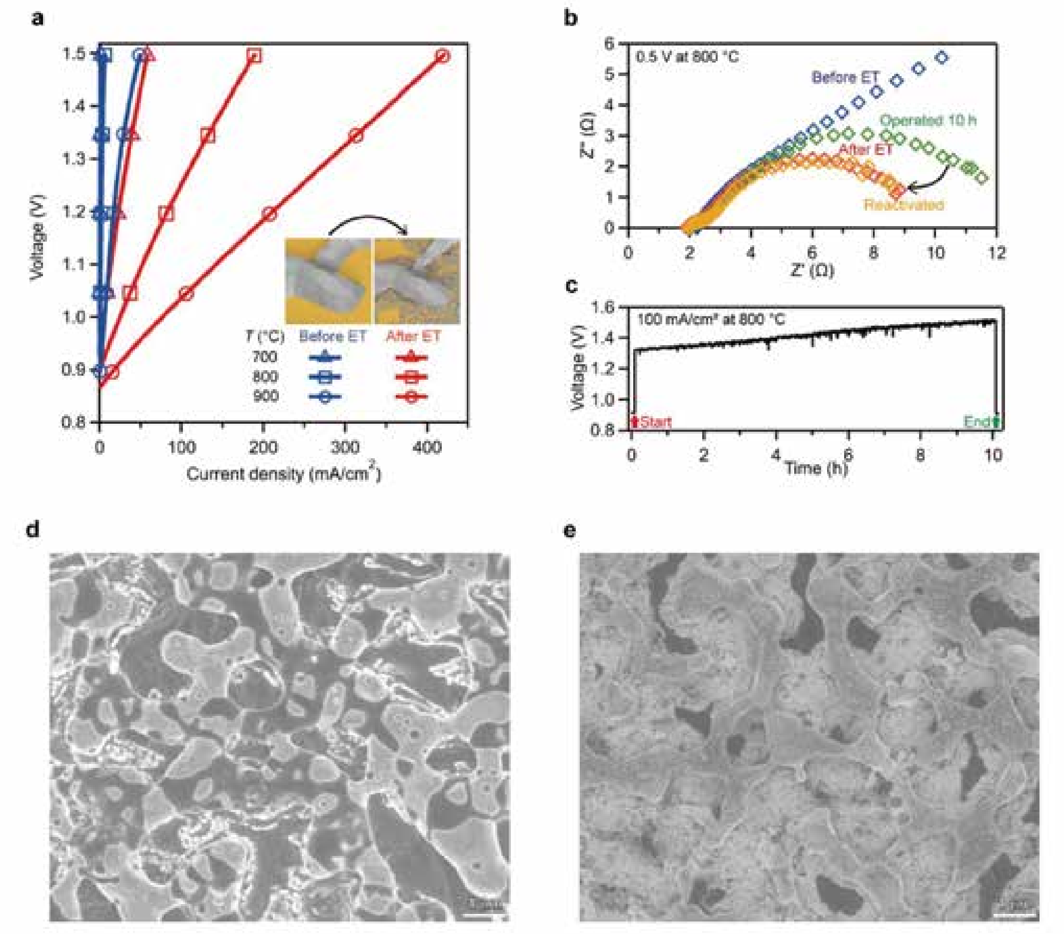

Fig. 4 Electrode performance before and after ET and its reactivation behavior by ET. a) The temperature-dependent *I–V* characteristics before and after ET; the current density increases with ET at all temperatures. b) Electrochemical impedance spectra recorded before ET (blue), after ET (red), after 10 h of operation (green), and after reactivation by ET (yellow) (see text for details). c) Voltage of the 3D nanocomposite electrode measured for 10 h under a constant current density of 100 mA cm^{-2} at 800 ℃. d,e) SEM image of the electrode after 10 h operation (d) and after reactivation by execution of ET (e). Insets in a are schematics of the electrodes before and after ET. The bright and dark regions in (d) and (e) corresponds to the Pt and YSZ, respectively

In order to examine the achieved degree of microstructuring and the associated cell output by ET, cell performances were investigated between 500 to 900 °C after the application of ET under three different voltages (V_{ET} = 1.6, 2.0, and 2.4 V) at 900 °C. The *I-V* characteristics measured at 800 °C are representatively shown in Fig. 5a, indicating an overall increase in their current densities with the magnitude of VET. This trend is maintained over the entire temperature range as evidenced by plotting the temperature dependence of the current density at 1.3 V, the voltage at which the endothermic heat from electrolysis is known to balance that from the Joule heating (Fig. 5b)[36]. Upon observation of the individual 3D nanocomposite structures in Fig. 2d and Fig. 5a, an increase in V_{ET} leads to decreased microparticle size and expansion of the area occupied by them, which are responsible for the current density enhancement. Furthermore, in contrast to the cell output before ET, a distinctive reduction in the temperature dependence of the current densities between 700 and 900 °C is observed by the application of ET regardless of V_{ET} (Fig. 5b). Namely, the slope in Fig. 5b decreased by 3.6 times from 0.075 to 0.021 $°C^{-1}$ between 800 and 900 °C. These enhanced

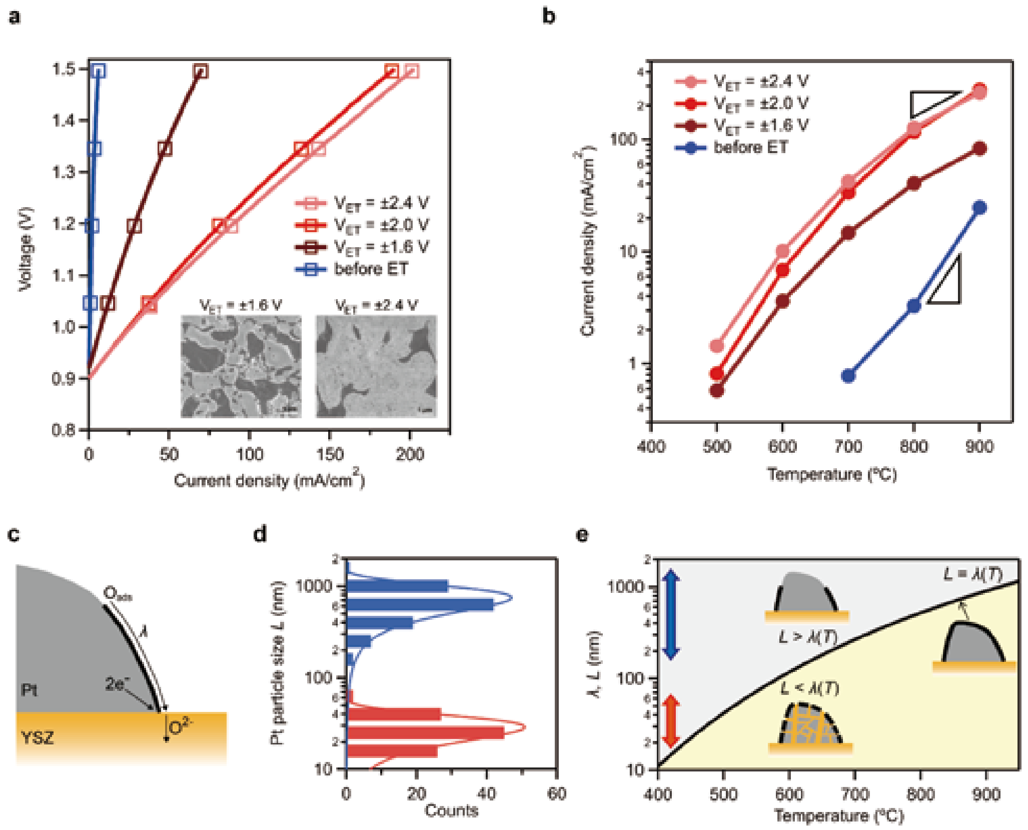

Fig. 5 The cell output dependence on the applied voltages during ET (V_{ET}), a schematic of the active site, and the relationship among the diffusion length λ (*T*) of the adsorbed oxygen atoms (O_{ads}) and the Pt particle size *L*. a) I-V characteristics at 800 ° C for three different V_{ET}s. Inset figures show the plan-view SEM images of the electrodes treated at V_{ET} = 1.6 V (left) and 2.4 V (right). b) Current density at +1.3 V for the nanostructured textile electrodes processed under different V_{ET}s. The gradients are illustrated by the two triangles (see text for details). c) Schematic of the active site illustrating the distance on the Pt surface over which O_{ads} can diffuse and be captured into the electrolyte. d) Histogram of the Pt particle size *L* before (top in blue) and after (bottom in red) ET under V_{ET} = 2.0 V, respectively. The two curves are Gaussian fits to the histograms. The mean *L* value reduced from 830 to 34 nm upon ET. e) The calculated λ (*T*), (solid curve) together with illustrations of the two regimes; *L* > λ (*T*), at which the TPB density is strongly temperature-dependent with inactive Pt surface remaining (top center inset), and *L* < λ(*T*), at which the TPB density is temperature-independent with the entire Pt surface activated (right inset). *L* < λ(*T*), is realized even at low temperatures for the 3D nanocomposite electrode due to the reduced *L* (bottom center inset). The vertical arrows indicate the range of *L* observed for the 2D network electrode (blue) and the 3D nanocomposite electrode (red)

current densities and the reduction in its temperature dependence induced by ET can be explained by comparing the Pt particle size L and the temperature-dependent diffusion length $\lambda(T)$ of the adsorbed oxygen atoms (O_{ads}) on the Pt surface (Fig. 5c)37)38). Taking V_{ET} = 2.0 V as an example, L was experimentally determined by systematically analyzing the SEM and STEM-EDS images in Fig. 2c and Fig. 3b, respectively (see Figure S3, Supporting Information for details). The mean L values obtained from the Gaussian fitting were 830 and 34 nm for the 2D network and the 3D nanocomposite electrodes, respectively (Fig. 5d). Given that the TPB is the effective region on the Pt electrode in which O_{ads} can access the electrolyte, $\lambda(T)$ dictates the TPB density. Assuming sufficient ionic conductivity in the electrolyte and an abundant supply of reactant molecules, $\lambda(T)$ takes the Arrhenius type function (see Supporting Information for details38)). By using the physical parameters reported by Yan *et al* 38)., we show the calculated $\lambda(T)$ in Fig. 5e, demonstrating its exponential increase with temperature, which suggests that the current density is significantly affected by the relationship between L and $\lambda(T)$. When $L > \lambda(T)$, only a limited portion of the Pt surface along the Pt/YSZ interface becomes active, causing the TPB density to increase with temperature, as scaled by $\lambda(T)$ (top center inset in Fig. 5c). This is exactly the case observed for the 2D network electrode before ET showing large temperature-dependent current densities. The calculated λ at 700 °C is 250 nm, which is much shorter than the mean L of 830 nm observed for the 2D network Pt electrode. The temperature required for $\lambda(T)$ to reach a mean L of 830 nm is ≈870 °C (top right inset in Fig. 5e). In contrast, when $L < \lambda(T)$, the TPB density is less dependent on temperature because the entire Pt surface becomes the active site, matching the experimental condition for the 3D composite electrode with L = 34 nm ≪ 250 nm, showing a reduced temperature dependence in its current density from 700 to 900 °C. Thus, the decrease in $\lambda(T)$ at lower temperatures can be counteracted by reducing L to satisfy the $L \leq \lambda(T)$ condition, which is realized in our 3D nanocomposite electrode after ET (bottom center inset in Fig. 5c). Indeed, for all V_{ET} tested, we were able to achieve the same current densities obtainable only above 700 °C before ET at a temperature as low as 500 °C after ET. This capability to decrease the operation temperature by 200 °C greatly expands the design of HTECs. Overall, a quantitative measure of the particle size with respect to the TPB density is given. We showed that the diffusion length of the surface oxygen atom $\lambda(T)$ sets the upper bound on TPB density, indicating that only a portion of the catalyst surface is utilized for the reaction in typical micrometer-sized catalysts. Reducing the catalyst particle size below $\lambda(T)$ to tens of nanometers by ET allows to use the entire catalyst particle surface efficiently.

3. Conclusion

In summary, we have demonstrated an effective approach to producing high-performance HTEC electrodes using cantaloupe-rind-inspired Pt nanostructured textiles taking a steam electrolysis cell as a model system. Subjecting this electrode to in situ AC voltage application at high temperature successfully led to the production of an ultrafine 3D nanocomposite structure made of Pt, Zr, and O. The 3D nanocomposite structure greatly increases the TPB density and enhances the current density which allows to reduce the operation temperature window by as much as 200 °C. Despite the inevitable aggregation of the Pt particles after high temperature operation, the continuous nature of our structure allows the reactivation of the electrode to its initial configuration through a simple voltage application on demand, providing a viable solution to one of the biggest challenges in HTECs and significantly extending their overall lifetimes39). Given the scalable fabrication process and the applicability to other major catalysts such as Au, palladium, transition metals, and their oxides40)–45),the use of this nanostructured textile on various oxide electrolytes combined with ET should serve as an effective process for the development of highly efficient HTEC electrodes. By fine-tuning the key variables in ET, including treatment temperature and ambient atmosphere, we anticipate that this versatile technology to impact not only steam electrolysis but also other energy conversion reactions. These include Pt-electrodes in micro-solid oxide fuel cells33), electrocatalytic electrodes for CO_2 reduction to hydrocarbon fuels46), and extend to other high-temperature devices such as sensor electrodes requiring high durability and sensitivity47)–49), thereby enhancing the performance of various devices.

4. Experimental Section

Fabrication of Pt Nanostructured Textile Electrode : 0.4 mL of an 8 wt.% polyvinylpyrrolidone (PVP, molecular mass 1,300,000 of ≈10,000 monomer units) methanol solution was fed using a syringe at a constant rate of 1 mL h^{-1} while applying a direct current (DC) voltage of 15 kV between the tip of the syringe and the square titanium (Ti) plate (area 25 cm^2) facing it 15 cm away to form the fibrous PVP sheet on the Ti-plate. Mass equivalent to 0.6 mg cm^{-2} of Pt was deposited on the fibrous PVP structure at a rate of 1 Å s^{-1} by radio-frequency magnetron sputtering (T857-1, CREATE DESIGN) in Ar at 10 Pa. The sputtering target was a 25 mm-phi × 1 mm-thick pure Pt disk (4N grade, TOSHIMA Manufacturing Co., Ltd.). The Pt-deposited PVP fibrous sheet was cut out into a 12 mm-phi disk and immersed in ultrapure water to selectively dissolve the PVP for releasing the Pt nanostructured textile electrode. All processes were conducted at room temperature.

Fabrication of High-Temperature Cell : The electrolyte was prepared by pressing an 8 at.% yttria-doped zirconia powder (TZ-8YSB, TOSO) into a 25 mm-phi × 0.6 mm-thick disk at a pressure of 100 MPa at room temperature. Subsequently, the disk was sintered in the ambient atmosphere at 1500 °C for 2 h and mirror-polished on both sides, giving a dense disk with a diameter of 20 mm and a thickness of 0.4 mm. One surface was spin-coated at 600 rpm with a slurry containing 50 wt.% Gd-added CeO_2 powder (GDC-10, DAIICHI KIGENSO KAGAKU KOGYO K.K.) in an ethyl cellulose solution (EC-200FTP, Nisshin Kasei Co., Ltd.) dispersed in ethanol. After firing the spin-coated disk at 1200 °C for 3 h in an ambient atmosphere, a slurry containing 50 wt.% $La_{0.6}Sr_{0.4}Fe_{0.8}Co_{0.2}O_{3-d}$ powder dispersed in an ethyl cellulose solution (EC-200FTP, Nisshin Kasei Co., Ltd.) was screen-printed (ST80-18-25, Tokyo Process Service Co., Ltd.) on the spin-coated surface to a diameter of 6 mm and a thickness of 10 μm. The disk was again fired for 2 h at 1100 °C in an ambient atmosphere. Two stacked pieces of Pt nanostructured textile electrode with a diameter of 12 mm were attached to the uncoated side of the YSZ disk at room temperature.

Electrochemical Measurements:Electrochemical measurements were carried out using a custom-made setup consisting of two concentric alumina tubes housed inside a vertical tube furnace (Figure S4, Supporting Information). The inner tube provides the gas to the cathode consisting of 10% water vapor and 3.8% hydrogen balanced by N_2. The gas flow rate was set to 50 sccm before the heating and kept constant throughout the series of measurements. The outer tube was sealed to the disk cell using ceramic glass (Aron Ceramic E, TOAGOSEI CO., LTD.), with the cathode facing the inner tube to prevent gas contamination on the anode. The electrical contacts to the two electrodes were made by pressing a Pt-mesh on each side of the disk cell as the current collectors. Each Pt-mesh was connected to a potentiostat (Modulab XM ECS, Solartron Analytical) with Au wires protected in alumina tubes. The anode was exposed to the ambient atmosphere. The temperature was increased up to the measurement temperature at a rate of 10 °C min^{-1}. The I–V characteristics were measured at a sweep rate of 50 mV s^{-1} at the measurement temperature. At 800 °C, a constant electric field of +1.3 V was applied, and the composition of the generated gas was analyzed using gas chromatography (GC490, Agilent Technologies). The results verified that the obtained current density was derived 100% from steam electrolysis and not from the decomposition of electrodes. A time sequence of the temperature and the electrochemical measurements are illustrated in Figure S5 (Supporting Information).

Electrical Treatments : Electrical treatments (ET) were carried out at 900 °C under the same atmospheric condition as that of the water vapor electrolysis reaction. A single ET cycle consisted of an application of a positive voltage of V_{ET} for 1 min followed by a negative voltage of -V_{ET} for 1 min. This cycle was repeated consecutively 20 times.

Microstructure Observation of the Cell : The SEM (S-4800, Hitachi High-Tech Corp.) characterization was conducted at an acceleration voltage of 5.0 kV and a current value of 15 μA. The observation was made at a low magnification of 10,000× and subsequently at a high magnification of 200,000×. STEM-EDS was conducted using ARM-300F (JEOL Ltd.) at an acceleration voltage of 300 kV and a current value of 15 μA. The Pt/YSZ interface regions of the cell for STEM-EDS were prepared by using a focused ion beam (ND-5000, Hitachi).

Electrical Resistivity Measurement : The room temperature in-plane resistivity of the Pt nanostructured textile electrodes was measured via the four-probe method using a VSP potentiostat (BioLogic Science Instruments) and a four-point probe with a needle spacing of 0.1mm pitch (NPS, SEP-04-WR-WP). Excitation currents of 50, 100, 150, 200, and 250 μA were applied and the voltage was measured to derive the resistivity of the samples.

Determination of Particle Size L : The particle size L was derived by analyzing the SEM and high-angle annular dark field (HAADF)-STEM images using the following generally accepted procedure 50). The contrast in the image was classified into bright and dark regions corresponding to Pt and YSZ, respectively. A vertical line was drawn over the image, and a point along this line where the contrast changed from dark to bright was defined as the edge of a Pt particle. The minimum distance from this edge to the point at which the contrast changed from bright to dark within the same particle was defined as L. This process was repeated until one hundred distances were obtained from each image by additionally drawing vertical and horizontal lines on Fig. 2c and Fig. 3b at spacings of 500 and 5 nm, respectively (Figure S3, Supporting Information).

References

1) J. Riegel, H. Neumann, H. M. Wiedenmann, *Solid State Ionics* **2002**, *152–153*, 783.
2) R. Moos, *Int. J. Appl. Ceram. Technol.* **2005**, *2*, 401.
3) A. B. Stambouli, E. Traversa, *Renewable Sustainable Energy Rev.* **2002**, *6*, 433.
4) A. Hauch, R. Küngas, P. Blennow, A. B. Hansen, J. B. Hansen, B. V. Mathiesen, M. B. Mogensen, *Science* **2020**, *370*, eaba6118.
5) Y. Song, X. Zhang, K. Xie, G. Wang, X. Bao, *Adv. Mater.* **2019**, *31*, 1902033.
6) J. T. S. Irvine, D. Neagu, M. C. Verbraeken, C. Chatzichristodoulou, C. Graves, M. B. Mogensen, *Nat. Energy* **2016**, *1*, 15014.
7) M. B.Mogensen,M. Chen, H. L. Frandsen, C. Graves, A. Hauch, P. V. Hendriksen, T. Jacobsen, S. H. Jensen, T. L. Skafte, X. Sun, *Fuel Cells* **2021**, *21*, 415.
8) F. Monaco, M. Hubert, J. Vulliet, J. P. Ouweltjes, D. Montinaro, P. Cloetens, P. Piccardo, F. Lefebvre-Joud, J. Laurencin, *J. Electrochem. Soc.* **2019**, *166*, F1229.
9) M. Trini, P. S. Jørgensen, A. Hauch, J. J. Bentzen, P. V. Hendriksen, M. Chen, *J. Electrochem. Soc.* **2019**, *166*, F158.
10) Y.Wang, C. Wu, B. Zu, M. Han, Q. Du,M.Ni, K. Jiao, *J. Power Sources* **2021**, *516*, 230660.
11) M. Rosa, P. Zielke, R. Kiebach, V. Costa Bassetto, A. Lesch, V. Esposito, *J. Eur. Ceram. Soc.* **2019**, *39*, 1279.
12) R. Nishida, P. Puengjinda, H. Nishino, K. Kakinuma, M. E. Brito, M. Watanabe, H. Uchida, *RSC Adv.* **2014**, *4*, 16260.
13) E. A. Holm, S. M. Foiles, *Science* **2010**, *328*, 1138.
14) Y. Itagaki, J. Cui, Y. Tani, H. Aono,H. Yahiro, *ECS Trans.* **2019**, *91*, 1963.
15) C. R. He, W. G. Wang, *Fuel Cells* **2009**, *9*, 630.
16) T. Ryll, H. Galinski, L. Schlagenhauf, P. Elser, J. L. M. Rupp, A. Bieberle-Hutter, L. J. Gauckler, *Adv. Funct. Mater.* **2011**, *21*, 565.
17) L. Zhang, X. Li, J. Lu, L. Zhang, S. Hu, H. Gong, X. Liu, B. Mao, X. Zhu, Z. Liu, W. Yang, *Nano Lett.* **2021**, *21*, 6952.
18) D. Kim, G. Dimitrakopoulos, B. Yildiz, *J. Am. Chem. Soc.* **2022**, *144*, 21926.
19) S. Higashi, T. Tachikawa, K. Oh-ishi, K. Shigetoh, K. Takechi, A. Beniya, *J. Mater. Chem. A* **2020**, *8*, 25061.
20) S. Higashi, T. Matsui, A. Beniya, *ACS Appl. Mater. Interfaces* **2022**, *14*, 40214.
21) S. Higashi, A. Beniya, *Appl. Catal., B* **2023**, *321*, 122030.
22) H. Pöpke, E. Mutoro, B. Luerssen, J. Janek, *J. Phys. Chem. C* **2012**, *116*, 1912.
23) S. P. Yoon, S. W. Nam, S.-G. Kim, S.-A. Hong, S.-H. Hyun, *J. Power Sources* **2003**, *115*, 27.
24) G. Tao, K. R. Sridhar, C. L. Chan, *Solid State Ionics* **2004**, *175*, 621.
25) L. Bultel, C. Roux, E. Siebert, P. Vernoux, F. Gaillard, *Solid State Ionics* **2004**, *166*, 183.
26) V. Srot, M. Watanabe, C. Scheu, P. A. van Aken, U. Salzberger, B. Luerßen, J. Janek, M. Rühle, *Solid State Ionics* **2010**, *181*, 1616.
27) J. J. Bentzen, J. V. T. Høgh, R. Barfod, A. Hagen, *Fuel Cells* **2009**, *9*, 823.
28) R. Fernández-González, E. Hernández, S. Savvin, P. Núñez, A. Makradi, N. Sabaté, J. P. Esquivel, J. C. Ruiz-Morales, *J. Power Sources* **2014**, *272*, 233.
29) J. A. Moulijn, A. E. van Diepen, F. Kapteijn, *Appl. Catal., A* **2001**, *212*, 3.
30) R. M. German, Crit. Rev. *Solid State Mater. Sci.* **2010**, *35*, 263.
31) A. T. Burkov, A. Heinrich, P. P. Konstantinov, T. Nakama, K. Yagasaki, *Meas. Sci. Technol.* **2001**, *12*, 264.
32) J. Nielsen, T. Jacobsen, *Solid State Ionics* **2007**, *178*, 1001.
33) T. Park, G. Y. Cho, Y. H. Lee, W. H. Tanveer, W. Yu, Y. Lee, Y. Kim, J. An, S. W. Cha, *Int. J. Hydrogen Energy* **2016**, *41*, 9638.
34) E. Mutoro, S. Günther, B. Luerßen, I. Valov, J. Janek, *Solid State Ionics* **2008**, *179*, 1835.
35) B. Scherrer, M. Döbeli, P. Felfer, R. Spolenak, J. Cairney, H. Galinski, *Adv. Mater.* **2015**, *27*, 6220.
36) Q. Li, Y. Zheng, W. Guan, L. Jin, C. Xu, W. G. Wang, *Int. J. Hydrogen Energy* **2014**, *39*, 10833.
37) J. Mizusaki, K. Amano, S. Yamauchi, K. Fueki, *Solid State Ionics* **1987**, *22*, 323.
38) Y. Yan, S. C. Sandu, J. Conde, P. Muralt, *J. Power Sources* **2012**, *206*, 84.
39) C. Graves, S. D. Ebbesen, S. H. Jensen, S. B. Simonsen, M. B. Mogensen, *Nat. Mater.* **2015**, *14*, 239.
40) J. G. Lee, J. H. Park, Y. G. Shul, *Nat. Commun.* **2014**, *5*, 4045.
41) Y. Choi, H.-J. Cho, J. Kim, J.-Y. Kang, J. Seo, J. H. Kim, S. J. Jeong, D.-K. Lim, I.-d. Kim, W. Jung, *ACS Nano* **2022**, *16*, 14517.
42) Y. Chen, Y. Bu, Y. Zhang, R. Yan, D. Ding, B. Zhao, S. Yoo, D. Dang, R. Hu, C. Yang, M. Liu, *Adv. Energy Mater.* **2017**, *7*, 1601890.
43) J. Y. Koo, Y. Lim, Y. B. Kim, D. Byun, W. Lee, *Int. J. Hydrogen Energy* **2017**, *42*, 15903.
44) G. Yu, T. S. Li, M. Xu, M. Andersson, B. Li, H. Tang, J. Parbey, J. Shao, *J. Alloys Compd.* **2017**, *693*, 1214.
45) T. Larsson, T. S. Li, M. Xu, I. Fransson, G. Yu, M. Andersson, B. Li, B. Sunden, *Mater. Res. Bull.* **2017**, *86*, 38.
46) B. Hu, V. Stancovski, M. Morton, S. L. Suib, *Appl. Catal., A* **2010**, *382*, 277.
47) J.-C. Yang, P. K. Dutta, *Sens. Actuators, B* **2007**, *125*, 30.
48) Y. Liu, J. Parisi, X.-C. Suna, Y. Lei, *J. Mater. Chem. A* **2014**, *2*, 9919.
49) S. C. Moulzolf, D. J. Frankel,M. Pereira da Cunha, R. J. Lad, *Microsyst. Technol.* **2014**, *20*, 523.
50) D. Bhattacharyya, A. Hajra, A. Basu, S. Jana, *Wear* **1977**, *42*, 63.

著者

日髙 重和
ひだか しげかず

マテリアル研究部
新規無機材料を起点としたエネルギー
変換技術の研究に従事

前川 佳史
まえがわ よしふみ

豊田中央研究所　博士 (工学)
ナノ粒子連結不織布を用いた触媒反応の
開発に従事

後藤 康友
ごとう やすとも

豊田中央研究所　博士 (工学)
ナノ粒子連結不織布を用いた触媒反応の
開発に従事

岡本 拓巳
おかもと たくみ

マテリアル研究部　博士 (工学)
新規無機材料を起点としたエネルギー
変換技術の研究に従事

東 相吾
ひがし しょうご

豊田中央研究所　博士 (理学)
ナノ粒子連結不織布を用いた触媒反応の
開発に従事

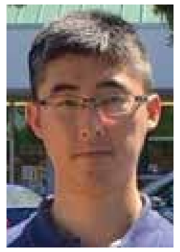

疋田 育之
ひきた やすゆき

マテリアル研究部　博士 (科学)
新規無機材料を起点としたエネルギー変換
技術の研究に従事